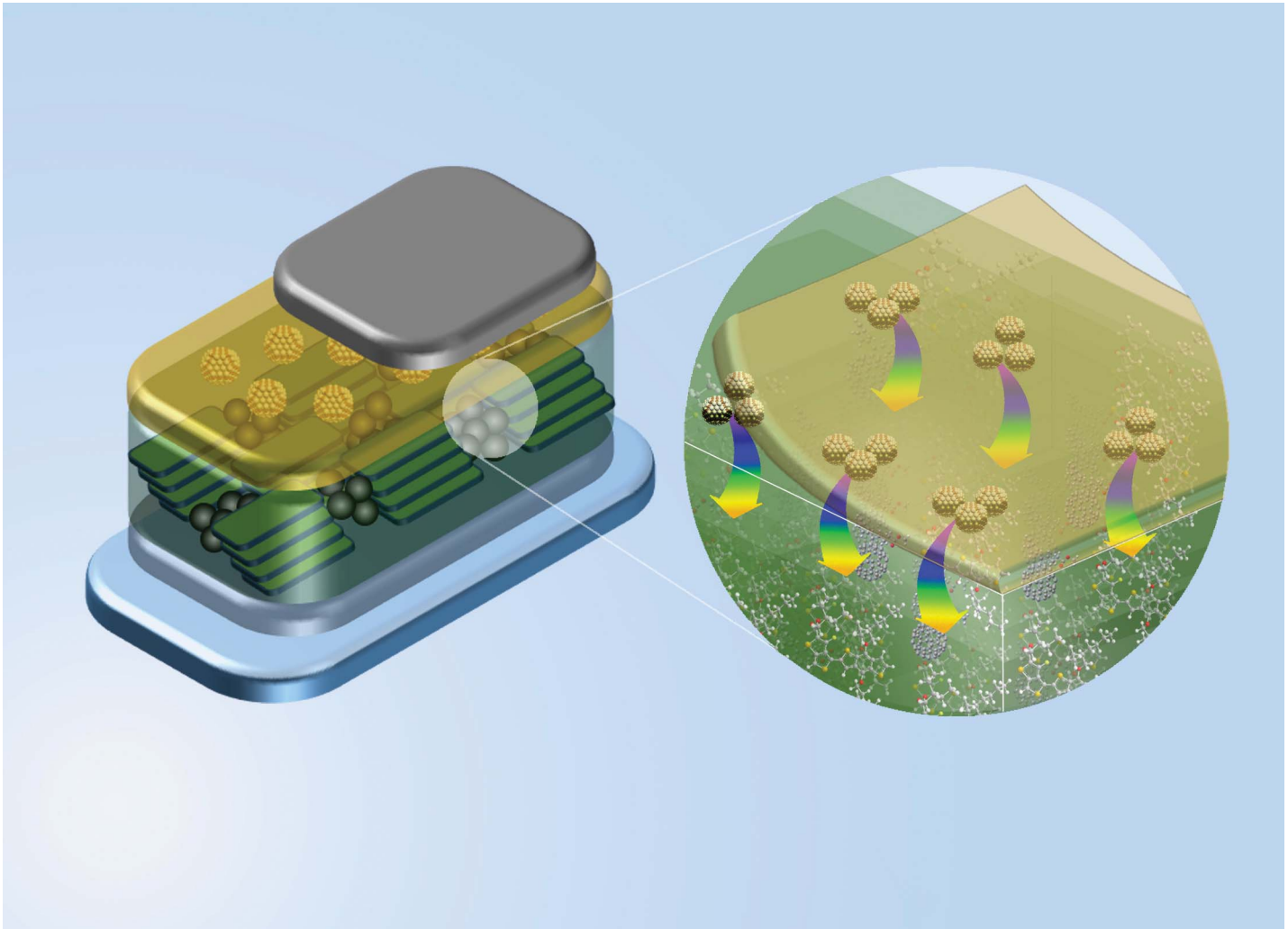

Showcasing a study on the fabrication of organic–inorganic hybrid solar cells through FRET by Dr Doo Kyung Moon at the Nano and Information Materials Lab at Konkuk University in Seoul.

Photon energy transfer by quantum dots in organic–inorganic hybrid solar cells through FRET

Organic–inorganic hybrid solar cells were fabricated with InP QDs in a BHJ active layer. InP QDs were distributed on the top of the hybrid active layer and showed strong emission characteristics. They played an important role in increasing J_{sc} by FRET to PTB7. By means of the synergistic effect between the InP QDs and the PFN interlayer, the performance of the device was enhanced.

As featured in:

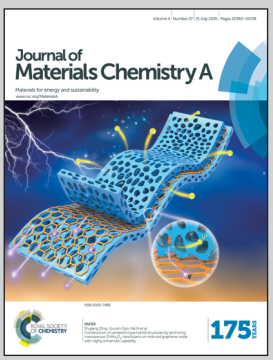

See Doo Kyung Moon *et al.*, *J. Mater. Chem. A*, 2016, **4**, 10444.

ROYAL SOCIETY OF CHEMISTRY

www.rsc.org/MaterialsA

Registered charity number: 207890

Journal of Materials Chemistry A

PAPER

View Article Online
View Journal | View Issue

Cite this: J. Mater. Chem. A, 2016, 4, 10444

Photon energy transfer by quantum dots in organic–inorganic hybrid solar cells through FRET†

Yong Woon Han,[a] Eui Jin Lee,[a] Jinwhan Joo,[b] Jongnam Park,[b] Tae Hyun Sung[c] and Doo Kyung Moon*[a]

Received 25th March 2016
Accepted 18th May 2016

DOI: 10.1039/c6ta02523d

www.rsc.org/MaterialsA

Organic–inorganic hybrid solar cells were fabricated with InP QDs (5 wt%) in a BHJ active layer (PTB7 + $PC_{71}BM$). InP QDs were distributed on the top of the hybrid active layer (BHJ + QDs), determined through XPS depth profiling and AFM analyses. InP QDs showed strong emission characteristics at λ_{max} = 650 nm in the PL spectra. They played an important role in increasing J_{sc} by Förster resonance energy transfer (FRET) to PTB7. The carrier recombination of the hybrid active layer (BHJ + QDs) was reduced by morphology control through introducing a PFN interlayer. The carrier mobility of the device with the hybrid active layer (BHJ + QDs) increased 1.5–1.58 times over that of the device with the BHJ active layer. By means of the synergy effect of InP QDs and the PFN interlayer, the PCE of the fabricated hybrid solar cells was enhanced from 4.9% (J_{sc} = 13.2 mA cm^{-2}, FF = 60.0%) to 8.4% (J_{sc} = 14.5 mA cm^{-2}, FF = 72.5%).

Introduction

Organic photovoltaics (hereinafter called OPVs) have advantages such as easy fabrication, low cost, flexibility, abundant availability, *etc.*, and have the potential to be used in the harvesting of renewable energy; therefore, they are being studied as an alternative energy source.[1] Recent OPV research has reported a power conversion efficiency (PCE) close to 10% for a polymer donor with high photon harvesting properties.[2]

Additionally, to record high efficiency with the device structure for OPVs, studies have been conducted on (1) additives for the phase separation between the polymer donor and the fullerene acceptor in the active layer,[3–6] (2) the introduction and control of an interlayer to improve the charge transporting characteristics,[7–13] (3) ternary structures[14–16] and tandem structures[17–19] for light absorption in a wide absorption range. However, despite these studies, the low absorption coefficient and low charge mobility of the polymer donor (organic semiconductor) are barriers to increasing the PCE. Furthermore, tandem structure cells, *etc.*, have the disadvantage that they require an additional and complicated process such as the introduction of an interconnection layer for preventing inter-mixing between the top cell and the bottom cell.

A study of hybrid solar cells has been recently reported, in which the correlation between organic semiconductors and inorganic semiconductors that can compensate for the limited absorption property and do not require a complicated process to overcome the drawbacks of the organic semiconductor was investigated.[20–23] Hybrid solar cells can be produced by mixing organic semiconductors and inorganic semiconductors in the active layer or introducing them in separate layers *via* a simple method.

Inorganic semiconductors or compound semiconductors have advantages such as a broad absorption range, high absorption coefficient, high conductivity and fast carrier mobility.[24–26] However, despite their advantages, inorganic solar cells require complex manufacturing processes and high production costs due to their insolubility. In particular, the thin film manufacturing process utilizing vacuum deposition and sputtering is limited in its application to the fabrication of organic–inorganic hybrid cells.

Among inorganic semiconductors, quantum dots (hereinafter called QDs) have recently received attention for their ability to overcome these disadvantages. In particular, a number of studies on LEDs and OPVs have been reported on the possibility of bandgap tuning due to the size of QDs and the types of ligands surrounding them.[27–31] QDs are available through solution process because they are dispersed in solvent due to the introduction of ligands. These characteristics allow for the fabrication of hybrid solar cells with organic semiconductors. Bawendi[32] *et al.* have reported a PCE of 8.55% through energy band alignment by controlling the ligands of lead sulfide (PbS) QDs. Sargent[33] *et al.* have reported a PCE of 8.92% by using a PbS QDs active layer and an n-PCBM interlayer.

[a]Department of Materials Chemistry and Engineering, Konkuk University, 1 Hwayang-dong, Gwangjin-gu, Seoul 05029, Republic of Korea. E-mail: dkmoon@konkuk.ac.kr

[b]School of Chemical Engineering, Ulsan National Institute of Science and Technology (UNIST), 100 Banyeon-ri, Ulsan, 44919, Republic of Korea

[c]Department of Electrical Engineering, Hanyang University, Wangsimni-ro, Seongdong-gu, Seoul 04763, Republic of Korea

† Electronic supplementary information (ESI) available. See DOI: 10.1039/c6ta02523d

There have recently been studies reported on hybrid solar cells, in which QDs were added to the active layer to increase the absorption property of the OPVs. Lee[20] *et al.* introduced PbS QDs with different bandgap energies (0.9–1.7 eV) instead of [6,6]-phenyl-C_{71}-butyric-acid methyl-ester (hereinafter called $PC_{71}MB$) as an electron acceptor with a polymer donor. They reported a PCE of 3.48% by producing hybrid solar cells in which poly[2,6-(4,40-bis(2-ethylhexyl)dithieno[3,2-*b*:20,30-*d*] silole)-*alt*-4,7(2,1,3-benzothiadiazole)] (PSBTBT) and PbS QDs were mixed. The electron transfer was explained by a comparison of the PL analysis and the energy level difference between the polymers and the QDs and the controlled carrier recombination through ligand exchange.

Guo[22] *et al.* reported a PCE of 6.94% by fabricating hybrid solar cells of poly[*N*-900-hepta-decanyl-2,7-carbazole-*alt*-5,5-(40,70-di-2-thienyl-20,10,30-benzothiadiazole)] (PCDTBT) and the fullerene derivative $PC_{71}BM$ with cadmium selenide (CdSe) QDs. CdSe QDs ($E_g = 1.7$ eV) were added to the active layer at a concentration of 1.09–6.54 wt% in 1,2-orthodichlorobenzene (ODCB). The mechanism of formation of the carriers, increased through the broad absorption property of CdSe QDs, was analyzed by transient absorption analysis. In other words, the photovoltaic performance improvements were explained by the direct electron transfer from the polymers to the QDs. However, carrier recombination occurred by direct contact with an electrode due to the rough morphology formed by the introduction of the QDs.

In our group, a high PCE of 8.4% has been achieved by fabricating the hybrid solar cells with an active layer, in which poly[[4,8-bis[(2-ethylhexyl)oxy]benzo[1,2-*b*:4,5-*b*′]dithiophene-2,6-diyl][3-fluoro-2-[(2-ethylhexyl)carbonyl]thieno[3,4-*b*]thiophenediyl]] (PTB7),[34,35] $PC_{71}BM$, and indium phosphide (InP) QDs[36] were mixed (hereinafter called BHJ + QDs). Unlike the results of Guo[22] *et al.*, the role of the InP QDs was confirmed to be in the photon energy transfer from the QDs to the polymers in the hybrid active layer (BHJ + QDs) in accordance with the energy level. In addition, InP QDs were distributed on the top of the BHJ active layer that was confirmed by X-ray photoelectron spectroscopy (XPS) depth profiling and atomic force microscopy (AFM) analyses. As a result, the morphology was controlled and carrier recombination was reduced by introducing the electron transport layer (ETL), which was confirmed by photoluminescence (PL) and space-charge-limited current (SCLC) analyses. By means of the synergy effect of InP QDs and the PFN interlayer, the photovoltaic properties were enhanced.

Experimental section

Materials

For the synthesis of InP QDs, indium acetate [$In(ac)_3$, 99.9%], *n*-trioctylphosphine (TOP, 90%), oleic acid (OA, 90%), and 1-octadecene (ODE, 90%) were purchased from Sigma-Aldrich (USA). Tris(trimethylsilyl)phosphine (TMSP, 10 wt% in hexane) was purchased from Strem. For the fabrication of hybrid solar cells, ITO glass (sheet resistance of 15 $\Omega\ \square^{-1}$) was purchased from GST materials (Korea). Poly(3,4-ethylenedioxythiophene):polystyrene sulfonic acid (PEDOT:PSS) (Clevious P VP AI 4083) was purchased from Heraeus (Germany) to introduce the hole transporting layer (HTL). PTB7 and $PC_{71}BM$ used as active materials and poly[(9,9-bis(30-(*N*,*N*-dimethylamino)propyl)-2,7-fluorene)-*alt*-2,7-(9,9-dioctylfluorene)] (PFN) used as the interlayer were purchased from 1-Material (Canada). 1,8-Diiodooctane (1,8-DIO), chlorobenzene (CB) and methanol were purchased from Sigma-Aldrich (USA).

Preparation of stock solution

For indium oleate [$In(OA)_3$] stock solution, $In(ac)_3$ (8 mmol) and OA (24 mmol) were placed in a 250 ml 3-neck round flask connected with a distilling condenser which had a vacuum adapter and a round flask. The round flask was cooled down with liquid nitrogen. The mixture was heated to 120 °C under vacuum below 70 mTorr for 2 h. After the mixture became a transparent liquid, it was cooled down to room temperature, followed by injection of ODE (72.4 ml). Finally the round flask was re-filled with argon gas.

Synthesis of InP core QDs

$In(OA)_3$ stock solution (5 ml) and OA (0.5 mmol) were placed in a 50 ml 3-neck round flask connected with a condenser. The flask was repeatedly evacuated and purged with Ar gas to provide a H_2O and O_2 free atmosphere. Then, the mixture was heated to 300 °C followed by injection of TMSP (4.3 mmol) and TOP (2 mmol) solution. The solution was kept at 300 °C for 30 min and cooled down to room temperature. To purify QDs, they were precipitated using ethanol and acetone and finally redispersed in chlorobenzene.

Device fabrication

For the fabrication of the hybrid solar cells, ITO glass was scribed to the size of 25 × 25 mm. ITO glass was cleaned by ultrasonication in the order of acetone, detergent, isopropanol and DI water, then UVO treatment (Ahtech LTS AH 1700) was carried out. The HTL (PEDOT:PSS) was spin coated at 4000 rpm for 30 s after filtering through a 0.45 mm PTFE filter and annealed at 140 °C for 10 min. BHJ active layer solution was fabricated with PTB7 and $PC_{71}BM$ at the ratio of 1 : 1.5 (25 mg ml^{-1}) in CB (1,8-DIO 3 vol%) with or without InP QDs (5 wt%). The prepared BHJ active layer solution was stirred at 60 °C overnight in a glove box. The BHJ active layer was spin coated on the HTL after filtering through the PTFE filter to a thickness of 70 nm. The PFN interlayer was spin coated on the BHJ active layer at 3000 rpm for 30 s after being filtered through the PTFE filter. Finally, the metal electrode was fabricated by a thermal deposition method. The devices were transferred to a high vacuum chamber (under 1×10^{-6} Torr) and the Al electrode was thermally deposited at a rate of 5 Å s^{-1} to a thickness of 100 nm. After that, a UV sealant was spread on the devices and exposed to UV for 3 min to cure sealant with cover glass for encapsulation.

Film and device characterization

Current density–voltage (*J*–*V*) characteristics and dark current characteristics of the fabricated hybrid solar cells were

measured using a Keithley 2400 source meter unit. The light source used was a solar simulator (Oriel, 1000 W) and the reference cell was calibrated under AM 1.5G under 100 mW cm^{-2}. The external quantum efficiency (EQE) characteristics of the hybrid solar cells were measured using a Polaronix K3100 IPCE measurement system (McScience). UV-Vis absorption and photoluminescence characteristics were measured using Agilent 8453 and Perkin Elmer LS55, respectively. The size, crystalline structure and energy level of InP QDs were measured by transmission electron microscopy (TEM, JEM-2100), X-ray diffraction (XRD, D/MAX 2500V) and ultraviolet photoelectron spectroscopy (UPS, ESCALAB 250XI), respectively. The surface morphology characteristics and cross-sectional depth profiling characteristics were measured by atomic force measurement (AFM, PSIA XE-100) and X-ray photoelectron spectroscopy (XPS, ULVAC-PHI 5000 VersaProbe, Phi(Φ)). The surface potential characteristics were measured by AFM with a Lock-in Amplifier. The surface energy and contact angle were measured by contact angle measurement (DSA100, KRUSS).

Results and discussion

In Fig. 1, the molecular structures of the organic polymer donor PTB7 (Fig. 1(a)), fullerene acceptor $PC_{71}BM$ (Fig. 1(b)) that was used as the photoactive layer and water/alcohol soluble conjugated polymer poly[(9,9-bis(30-(*N*,*N*-dimethylamino)-propyl)-2,7-fluorene)-*alt*-2,7-(9,9-dioctylfluorene)] (PFN) (Fig. 1(c)) that used as the interlayer material are shown.

Fig. 1(d) shows a schematic image of the inorganic donor InP QDs. Additionally, Fig. 1(e) shows a schematic diagram of the cells fabricated using the conventional structure (ITO/PEDOT:PSS/active layer/PFN/Al). Device 1 is a bulk-heterojunction structure ([PTB7 + $PC_{71}BM$], BHJ). In contrast, Device 2 is a bulk-heterojunction structure ([PTB7 + InP QDs + $PC_{71}BM$], BHJ + QDs) into which the InP QDs were introduced. Devices 3 and 4 were fabricated as structures in which the PFN interlayer was introduced into Device 1 and Device 2 as the ETL.

The UV-Vis absorption spectra of PTB7 and InP QDs and the photoluminescence spectra of InP QDs are shown in Fig. 2(a). PTB7 is well known to show a maximum absorption peak at λ_{max} = 680 nm. However, the absorption peak onset of the InP QDs was found at λ = 660 nm and they have a bandgap energy of 1.70 eV. The wide band gap of the InP QDs indicates broad wavelength absorption (especially short wavelength absorption). In the UV-Vis absorption spectra, the InP QDs mainly absorb short wavelength light and relatively little long wavelength light.

In particular, the InP QDs show strong emission characteristics at λ_{max} = 650 nm in the PL spectra, which is consistent with the absorption property (λ = 500–700 nm) of PTB7. This means that InP QDs fully perform the role of a donor in transferring extra photon energy to PTB7 in the hybrid active layer (BHJ + QDs). The ultraviolet photoelectron spectroscopy (UPS) characteristics of InP QDs are shown in Fig. S1.† The valence band energy is determined to be the difference between the high and low kinetic energy cut-offs.[37,38]

$$E_{HOMO} = h\nu - (E_{cut\text{-}off} - E_{onset}) \quad (1)$$

The valence band level is 6.06 eV, as determined by eqn (1), and the conduction band level calculated by the bandgap energy (E_g = 1.7 eV) is 4.34 eV.

The X-ray diffraction (XRD) pattern and transmission electron microscopy (TEM) image of the InP QDs are shown in Fig. 2(b). The three main peaks were measured to be 26.3°, 43.6°, and 51.6°, respectively, and these values correspond to

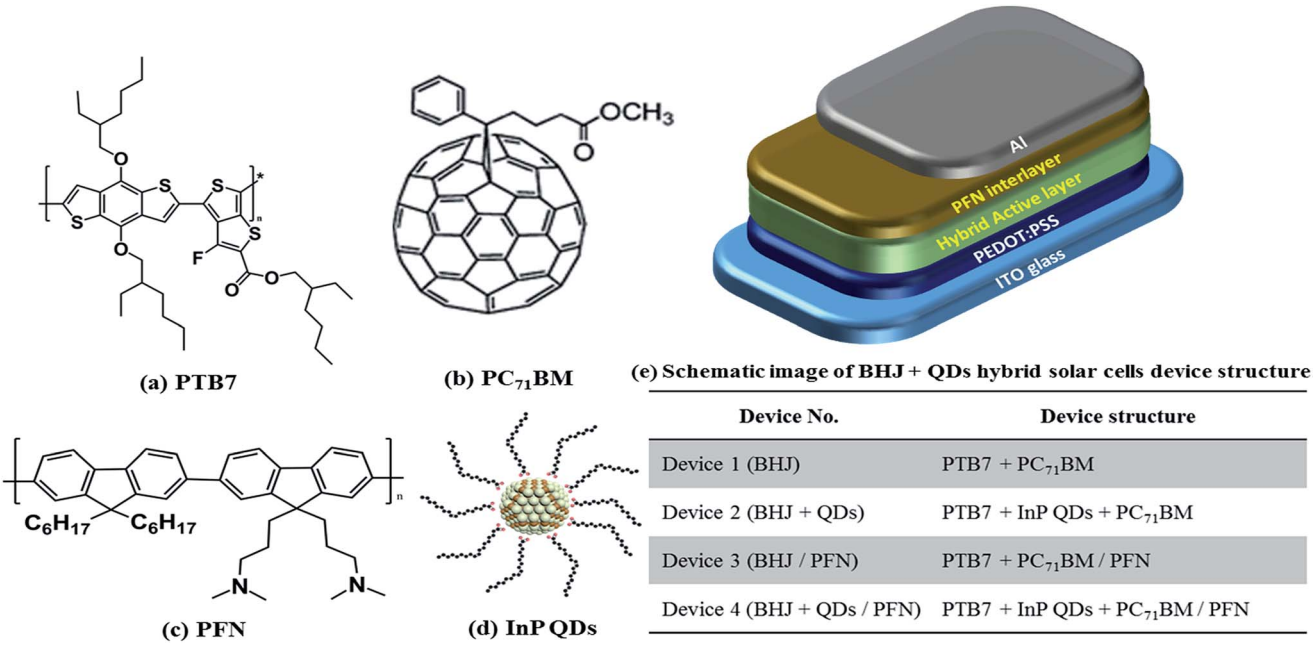

(e) Schematic image of BHJ + QDs hybrid solar cells device structure

Device No.	Device structure
Device 1 (BHJ)	PTB7 + $PC_{71}BM$
Device 2 (BHJ + QDs)	PTB7 + InP QDs + $PC_{71}BM$
Device 3 (BHJ / PFN)	PTB7 + $PC_{71}BM$ / PFN
Device 4 (BHJ + QDs / PFN)	PTB7 + InP QDs + $PC_{71}BM$ / PFN

Fig. 1 Chemical structure of (a) PTB7, (b) $PC_{71}BM$, (c) PFN, (d) InP QDs and (e) schematic image of BHJ + QD hybrid solar cell device structure.

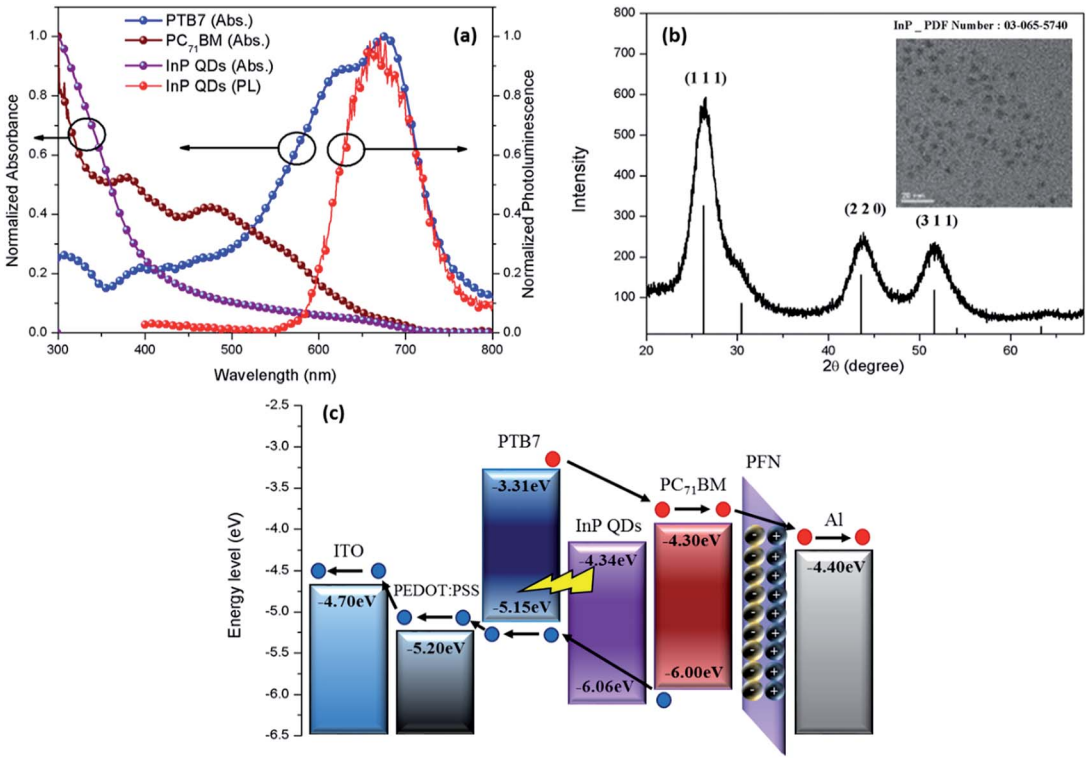

Fig. 2 (a) UV-Vis absorption spectra of PTB7, InP QDs, $PC_{71}BM$ and photoluminescence spectra of InP QDs, (b) X-ray diffraction (XRD) pattern and transmission electron microscopy (TEM) image of InP QDs and (c) energy band diagram of hybrid solar cells.

the (100), (220), and (311) planes of the InP QDs (the International Centre for Diffraction Data (ICDD) Powder Diffraction File (PDF), PDF#. 03-065-5740, zinc blend structure).[39,40] From Fig. 2(b), the average particle size of the InP QDs was found to be 4.3 nm, and they showed high crystallinity.

The highest occupied molecular orbital (HOMO), lowest unoccupied molecular orbital (LUMO), valence band and conduction band of the component materials used in the devices and the energy band diagrams are shown in Fig. 2(c).[9] At this time, the conduction band of the InP QDs was slightly lower than the LUMO of $PC_{71}BM$. This indicates that unlike PTB7, it is difficult for InP QDs to directly transfer electrons to $PC_{71}BM$. This result is consistent with the performance of the fabricated devices in which the InP QDs and $PC_{71}BM$ were mixed in the active layer. As shown in Fig. S2 and Table S1,† the device performance of the hybrid active layer (InP QDs + $PC_{71}BM$) showed a very low PCE value under 0.02%.

The current density–voltage (J–V) characteristics (Fig. 3(a)) and external quantum efficiency (EQE) characteristics (Fig. 3(b)) of conventional structure (ITO/PEDOT:PSS/active layer/PFN/Al) devices under 1 sun AM 1.5G irradiation at 93 mW cm^{-2} are shown in Fig. 3, and these results are summarized in Table 1.

As shown in Table 1, Device 1 using only Al electrodes on the BHJ active layer gave a PCE of 4.9% (J_{sc} = 13.2 mA cm^{-2}, V_{oc} = 0.575 V, FF = 60.0%). The PCE of Device 2 for which InP QDs were introduced into the active layer of Device 1 was 6.4% (J_{sc} = 13.9 mA cm^{-2}, V_{oc} = 0.676 V, FF = 62.5%). The PCE of Device 3 for which the PFN interlayer was introduced into Device 1 was 7.6% (J_{sc} = 13.6 mA cm^{-2}, V_{oc} = 0.717 V, FF = 72.2%). There was a larger increase in J_{sc} for Device 2 (J_{sc} = 13.2 mA cm^{-2} → 13.9 mA cm^{-2}), in which the InP QDs were introduced into the active layer, than for Device 3 (J_{sc} = 13.2 mA cm^{-2} → 13.6 mA cm^{-2}), in which the PFN interlayer was introduced between the active layer and the Al cathode.

Rotello[41] *et al.* and Guo[42] *et al.* have reported that the emission energy of QDs can be transferred to the polymers in a composite structure using zinc selenide (ZnSe) QDs and carbon (C) QDs, respectively. As shown in Fig. 2(a), the increase in J_{sc} was due to the enhancement of the photon energy through energy transfer caused by the overlap of the emission (λ_{max} = 650 nm) band of InP QDs and the absorption band of PTB7.

The increase in J_{sc} due to the introduction of InP QDs in this study is the result of Förster resonance energy transfer (FRET) of the InP QD emission to PTB7. FRET is a photo-physical process in which energy is transferred from an energy donor molecule to an acceptor molecule, and the phenomenon occurs due to the overlapping of the emission spectrum of the energy donor molecule and the absorption spectrum of the energy acceptor molecule.[43] In other words, InP QDs transferred extra photon energy to PTB7, and this energy transfer improved the photovoltaic property.

Meanwhile, V_{oc} showed a slightly higher increase for Device 3 (V_{oc} = 0.575 V → 0.717 V), in which the PFN interlayer was introduced, than for Device 2 (V_{oc} = 0.575 V → 0.676 V), in which the QDs were introduced into the active layer. Wu[44] *et al.* have reported that a higher surface potential leads to higher V_{oc}

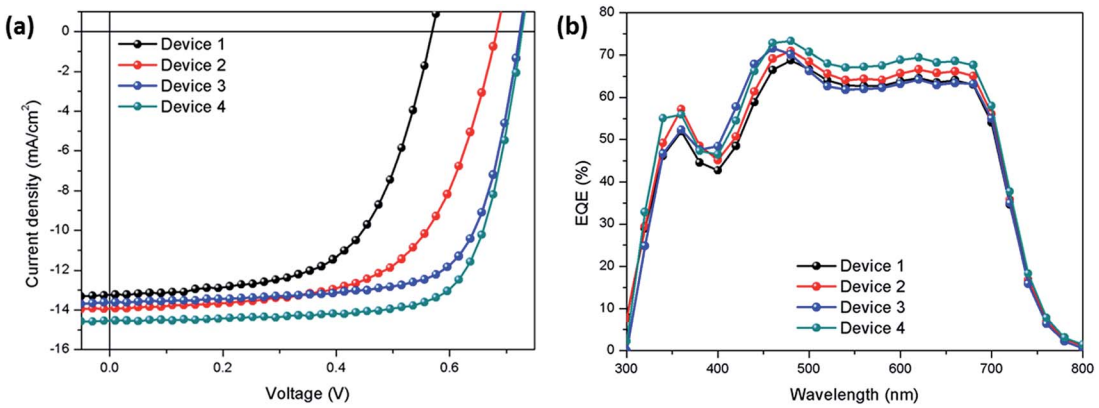

Fig. 3 Performance optimization of BHJ + InP QD hybrid solar cells: (a) current–density *versus* voltage (*J*–*V*) characteristics of conventional BHJ + InP QD hybrid solar cells under AM 1.5G illumination with an irradiation intensity of 93 mW cm^{-2}, (b) EQE spectra of BHJ + InP QDs hybrid solar cells.

Table 1 Photovoltaic performances of BHJ + InP QDs hybrid solar cells

Device structure	J_{sc} [mA cm^{-2}]	V_{oc} [V]	FF [%]	PCE [%]
Device 1 (BHJ/Al)	13.2	0.575	60.0	4.9[a]
Device 2 (BHJ + QDs/Al)	13.9	0.676	62.5	6.4[a]
Device 3 (BHJ/PFN/Al)	13.6	0.717	72.2	7.6[a]
Device 4 (BHJ + QDs/PFN/Al)	14.5	0.737	72.5	8.4[a]

[a] The average values and deviations were obtained from ten devices.

in terms of the built-in potential in conventional structure solar cells. As shown in Fig. S3,† the surface potential of the devices was 15.501 mV/1.598 mV (mean, R_q of (a) BHJ) and 30.484 mV/2.180 mV (mean, R_q of (d) BHJ + QDs/PFN interlayer). As a result, the higher surface potential leads to the enhancement of V_{oc}.

In particular, FF showed a higher increase for Device 3 (FF = 60% → 72.2%), in which the PFN interlayer was introduced, than for Device 2 (FF = 60% → 62.5%), in which the QDs were introduced into the active layer. Kim[45] *et al.* have reported that higher carrier recombination usually leads to lower FF. As shown in Fig. S4,† Devices 3 and 4 showed high FF because of low leakage current in the reverse bias region. This means the PFN interlayer retards carrier recombination. In other words, J_{sc} was improved by FRET; the extra photon energy was transferred from the InP QDs to PTB7, and the PFN interlayer caused the potential change of the surface and reduced the carrier recombination so that V_{oc} and FF were improved.[44,46]

The PCE of Device 4, in which both InP QDs and the PFN interlayer were introduced to Device 1, was 8.4% (J_{sc} = 14.5 mA cm^{-2}, V_{oc} = 0.737 V, FF = 72.5%). This corresponds to an approximately 71.4% increase compared to Device 1. The V_{oc} and FF were slightly increased compared to Devices 2 and 3, in which InP QDs and PFN interlayer were introduced, respectively. However, the J_{sc} was significantly increased (13.6 mA cm^{-2} → 14.5 mA cm^{-2}). This is the due to the synergistic effect of introducing InP QDs and PFN interlayer.

In other words, the J_{sc} was improved by FRET; the extra photon energy was transferred from the InP QDs to PTB7, and the PFN interlayer caused the potential change of the surface and reduced the carrier recombination so that the V_{oc} and FF improved.[44,46] Otherwise, the device performance showed the best results when 5 wt% InP QDs were added as shown in Fig. S5 and Table S2.†

In the EQE characteristics shown in Fig. 3(b), each Device 2–4 showed an increased area compared to Device 1. The J_{sc} can be calculated through the measurement of EQE, which can be defined as the amount of carriers generated from the active layer against the amount of photons supplied externally.[47–50] The calculated J_{sc} of Device 1 (BHJ/Al), Device 2 (BHJ + QDs/Al), Device 3 (BHJ/PFN/Al) and Device 4 (BHJ + QDs/PFN/Al) were 13.79, 14.24, 13.91, and 14.85 mA cm^{-2}, respectively. This is consistent with the J_{sc} increase shown in Table 1.

Fig. 4(a) shows the UV-Vis absorption spectra of the PTB7 layer and PTB7 and InP QDs (5 wt%) mixed layer with or without the PFN interlayer. The UV-Vis absorption spectra of the PTB7 + InP QDs layer showed an absorption peak (λ_{max} = 630, 680 nm) similar to the absorption spectra of the PTB7 layer, but the absorption intensity was increased in all areas. As shown in Fig. 2(a), this result is consistent with the effect of energy transfer by the overlapping of the emission of InP QDs and the absorption of PTB7. However, the introduction of the PFN interlayer on the PTB7 + InP QDs layer showed a slightly increased absorption property between 350 and 400 nm.[51,52] These results provide an understanding that the increased PCE was caused by the improvement in J_{sc}, and this is the synergy effect of the InP QDs and the PFN interlayer shown in Table 1.

Fig. 4(b) shows the UV-Vis absorption spectra under the condition that $PC_{71}BM$ was added to the active layer under the same conditions as Fig. 4(a). The absorption spectra of the samples were similar to those depicted in Fig. 4(a). However, the absorption peak under λ = 650 nm increased due to the absorption of $PC_{71}BM$ (depicted in Fig. 2(a)).

As shown in Table 1 and Fig. 3, this is consistent with the result indicating that the J_{sc} was significantly improved in the

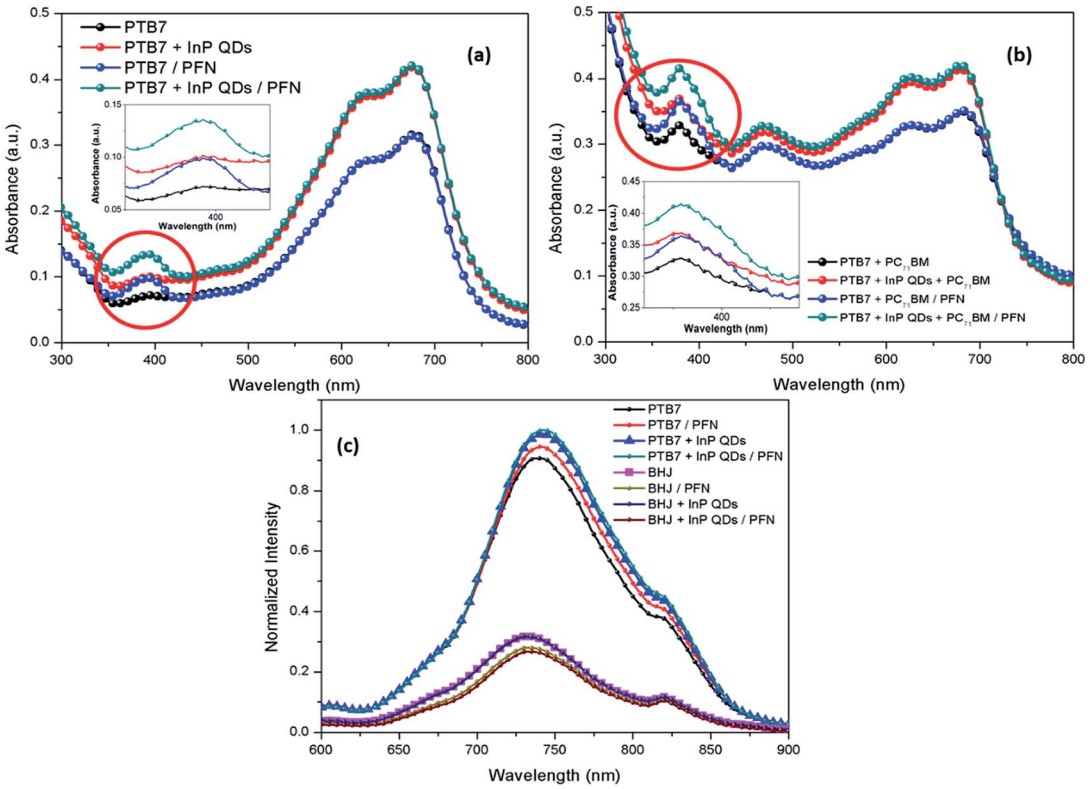

Fig. 4 Optical properties. UV-Vis absorption spectra of (a) PTB7, PTB7 + InP QDs and PTB7 + InP QDs with and without the PFN interlayer, (b) BHJ, BHJ + InP QDs and BHJ + InP QDs with and without the PFN interlayer, (c) PL spectra of the BHJ active layer and BHJ + InP QDs hybrid active layer with and without the PFN interlayer.

case where InP QDs (J_{sc} = 13.2 mA cm^{-2} → 13.9 mA cm^{-2}) or both InP QDs and a PFN interlayer (J_{sc} = 13.2 m A cm^{-2} → 14.5 mA cm^{-2}) were introduced. InP QDs greatly contributed to the improvement of J_{sc} through an increase in absorption in the hybrid active layer (BHJ + QDs), and the PFN interlayer contributed to the improvement in FF through a decrease in carrier recombination.

As shown in Fig. 4(c), the cases where InP QDs were introduced into PTB7 showed higher PL intensity rather than those without InP QDs. Therefore, this property resulted from excitons that were formed by carriers which was increased by InP QDs through energy transfer. This result is consistent with the high J_{sc} of Device 4 shown in Table 1. Similarly, the increased PL characteristics compared to PTB7 are due to the increased amount of excitons generated by the improved absorption.[53]

However, BHJ and the hybrid active layer (BHJ + QDs) where $PC_{71}BM$ was added to PTB7 and PTB7 + InP QDs active layer showed a low PL intensity. This is because the excited and separated electrons were accepted by $PC_{71}BM$. There were obvious variations in PL intensity among the blends of PTB7:$PC_{71}BM$ with or without the PFN interlayer (only small variations in PTB7:$PC_{71}BM$ with or without InP QDs). This means that InP QDs contributed to enhancing the absorbance property through energy transfer and the PFN interlayer contributed to reducing carrier recombination through carrier transfer.

As shown in Table 2, the PL quenching rate was the highest (73.2%) in the hybrid active layer (BHJ + QDs) in which InP QDs were added into the BHJ active layer and the PFN interlayer was introduced. Vandewal[54] *et al.* have described PL quenching as the separation of excitons at the donor–acceptor interface after the generation of carriers in the photoactive layer and transfer of the carriers to an external circuit. In other words, a high PL quenching rate contributes to an increase of J_{sc} *via* the quick movement of carriers from the BHJ active layer to an external circuit. This is consistent with the result that Device 4, shown in Table 1, had the highest efficiency. In other words, as shown in Fig. 2(c) and 3(a), this is a result of increase in the formation of carriers due to the energy transfer because the emission (λ_{max} = 650 nm) of the InP QDs overlapped with the absorption of PTB7. In addition, the PFN interlayer increased the FF and improved the PCE by reducing the recombination of the carriers.

Table 2 Photoluminescence quenching rate of the BHJ + InP QDs hybrid active layer

Condition	PL quenching rate (%)
PTB7 → BHJ	65.0
PTB7 + PFN → BHJ + PFN	70.3
PTB7 + InP QDs → BHJ + InP QDs	67.9
PTB7 + InP QDs + PFN → BHJ + InP QDs + PFN	73.2

Electron and hole mobility results by the SCLC method are shown in Fig. S6.† The current density (J) and voltage (V) were measured using an electron-only device (ITO/ZnO/active layer/PFN/Al) and a hole-only device (ITO/PEDOT:PSS/active layer/MoO_3/Ag). Mobility (μ) was calculated by applying the measured values to the Mott–Gurney space-charge-limited current formula, eqn (2):[55,56]

$$J = (9/8)\mu\varepsilon_0\varepsilon_r(V^2/L^3) \quad (2)$$

where μ: charge carrier mobility, ε_0: free-space permittivity, ε_r: dielectric constant of the semiconductor, V: applied voltage, L: thickness of the semiconductor layer.

As shown in Table 3, the electron mobilities of devices with the hybrid active layer (BHJ + QDs) and the BHJ active layer were calculated to be 3.10×10^{-3} cm^2 V^{-1} s^{-1} and 2.13×10^{-3} cm^2 V^{-1} s^{-1}, respectively. In addition, the hole mobilities were calculated to be 2.20×10^{-3} cm^2 V^{-1} s^{-1} and 1.39×10^{-3} cm^2 V^{-1} s^{-1}. The carrier mobility of the device with the hybrid active layer (BHJ + QDs) increased 1.5–1.58 times over that of the device with the BHJ active layer.

In other words, this is consistent with the results given in Fig. 4, which shows that addition of InP QDs increased the carriers in the active layer by means of photon energy transfer from the QDs to the polymers. Additionally, this is a result of the PFN interlayer effectively retarding carrier recombination, which is consistent with the high efficiency of Device 4 shown in Table 1.

The AFM morphology characteristics of the BHJ (Fig. 5(a)) active layer and the hybrid active layer (BHJ + QDs) (Fig. 5(b)) are shown in Fig. 5. Fig. 5(c) shows the morphology when the PFN interlayer is introduced into the hybrid active layer shown in Fig. 5(b). As shown in Fig. 5(a), the BHJ active layer formed a very uniform morphology with a root mean square (RMS) roughness of 1.36 nm. In Fig. 5(b), the hybrid active layer (BHJ + QDs) shows the morphology of a protruding probe with an RMS roughness of 1.63 nm.

In Device 2, FF slightly increased compared to the largely increased J_{sc} and V_{oc} with rough morphology. In the top of the hybrid active layer, QDs act as recombination centers because of the direct contact of the hybrid active layer with the electrode.

However, in Fig. 5(c), the introduction of the PFN interlayer resulted in a smooth morphology again with an RMS roughness of 1.53 nm. In Device 3, FF largely increased with uniform morphology compared to that in Device 2. This large increase caused by retarding the carrier recombination of the PFN interlayer is shown in Fig. S4.† This is a result of the PFN interlayer passivating the surface of the hybrid active layer (BHJ + QDs) on which the InP QDs are distributed. This indicates good interfacial adhesion between the active layer and the cathode, and it fits well with the results that PCE was improved by the increase in the J_{sc} and FF in Device 4 shown in Table 1.

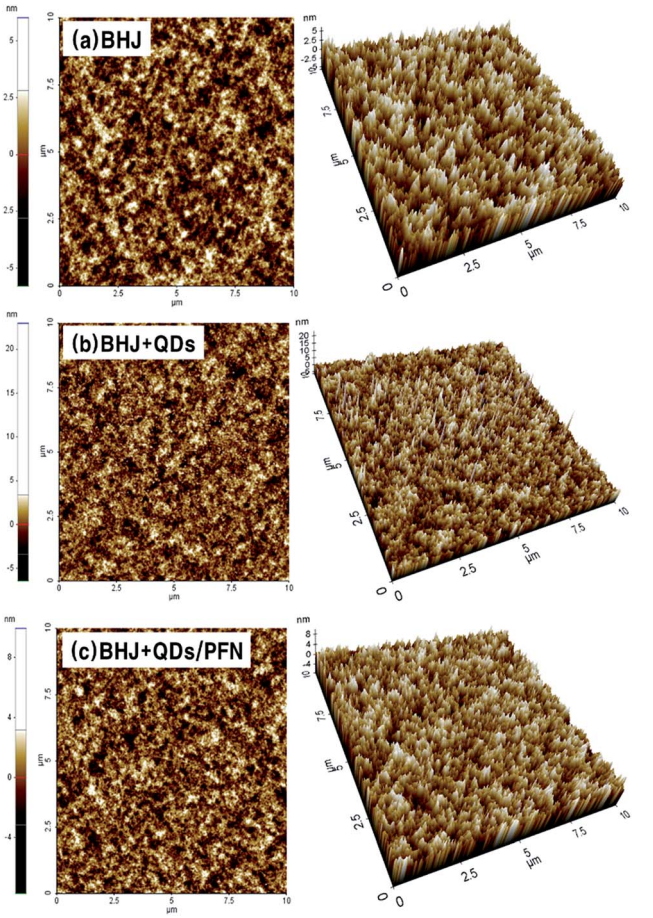

Fig. 5 AFM image of (a) BHJ active layer (reference), (b) BHJ + InP QDs hybrid active layer and (c) BHJ + InP QDs hybrid active layer with the PFN interlayer.

Table 3 Electron mobility and hole mobility of the active layer determined using the electron-only devices ITO/ZnO/PTB7 + $PC_{71}BM$ + InP QDs/Al and hole only devices ITO/PEDOT:PSS/PTB7 + $PC_{71}BM$ + InP QDs/MoO_3/Ag along with the use of the space charge current equation in the calculation

Conditions	μ_e [cm^2 V^{-1} s^{-1}]	μ_h [cm^2 V^{-1} s^{-1}]
PTB7 + $PC_{71}BM$	2.13×10^{-3}	1.39×10^{-3}
PTB7 + $PC_{71}BM$ + InP QDs	3.10×10^{-3}	2.20×10^{-3}

Fig. 6 shows the XPS depth profiling characteristics of the device (ITO/PEDOT:PSS/active layer), with the BHJ (Fig. 6(a)) and hybrid active layer (BHJ + QDs) (Fig. 6(b)). The measurement was conducted from 0 min (top of the active layer) to 90 min (bottom of the active layer) at a rate of 1 nm min^{-1}. The measured velocity was consistent with the thickness of the device (*ca.* 70–80 nm). Carbon (C) and sulfur (S) concentrations are a signal by existence of PTB7 and $PC_{71}BM$. As shown in Fig. 6(a), the C concentration rapidly decreased, but the indium (In) concentration sharply increased after 70 min. This is a result of reaching the surface of the ITO in 75 min (*ca.* 75 nm) by sputtering from the top of the active layer into the bottom of the active layer (ITO surface). In this case, the increase of S concentration after the 70 nm portion was a result of reaching the PEDOT:PSS layer.

However, Fig. 6(b) shows that an increase in the C concentration and a decrease in the In concentration occurred in 5 min. In addition, there was a similar trend, as shown in Fig. 6(a), after 60 min. This is a result of reaching the surface of

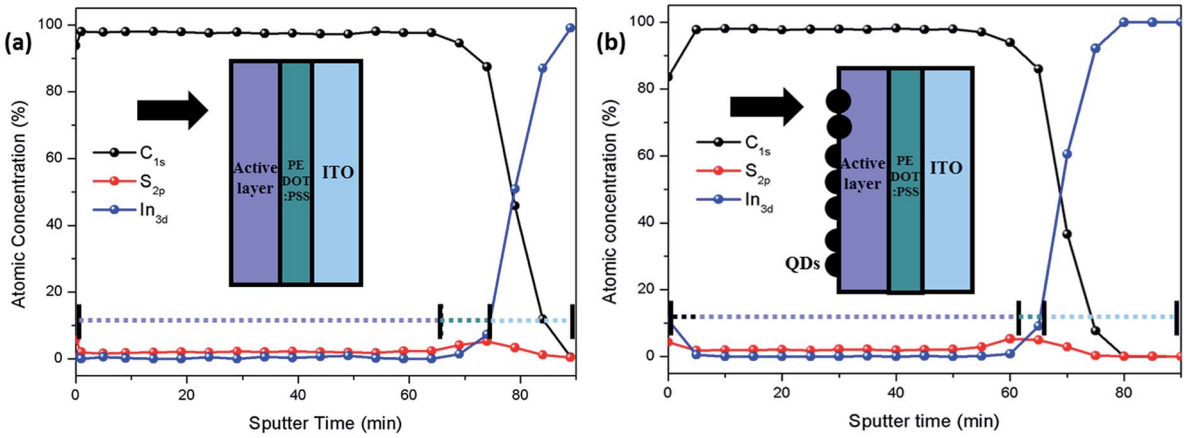

Fig. 6 XPS depth profiling image of (a) BHJ active layer (reference), (b) BHJ + QDs hybrid active layer.

the ITO in 65 min (*ca.* 65 nm), and most of the InP QDs are distributed on top of the active layer. This result is consistent with QDs being distributed on the top of the active layer mentioned above with the AFM characteristics in Fig. 5.

Generally, lower surface energy materials segregate into the air/film interface, while higher surface energy materials segregate into the film/electrode interface.[57] InP QDs were distributed on the top of the hybrid active layer because of the lower surface energy rather than PTB7 or $PC_{71}BM$ as shown in Fig. 6 and S7.† By means of this distribution, surface characteristics changed dramatically when the PFN interlayer was introduced onto the hybrid active layer.

Based on these results, as shown in Scheme 1, the InP QDs were distributed on the surface of the BHJ active layer, and directly came into contact with the electrode. Thus, the InP QDs could act as carrier recombination centers. However, the rough morphology and PCE could be improved through passivation by introducing a PFN interlayer.[58]

In our study, InP QDs increased the absorbance property as shown in Fig. 4. The PFN interlayer covered InP QDs distributed on the top of the hybrid active layer. The morphology changed more uniformly and the surface potential increased as shown in Fig. 5 and S3.† The PFN interlayer increased PL quenching characteristics and retarded carrier recombination as shown in Fig. 4(c) and S4.† Thus, Device 4 showed the best performance with the synergy effect of InP QDs and the PFN interlayer.

As a result, we revealed energy transfer through the structure of organic–inorganic hybrid solar cells in which InP QDs were introduced into the BHJ active layer (PTB7 + $PC_{71}BM$) and the energy diagram is shown in Scheme 1. Fabricated (BHJ + QDs) hybrid solar cells showed a structure similar to the ternary structure in terms of the energy band diagram.[59,60] However, unlike a ternary structure, InP QDs did not play a role in directly transferring electrons to the $PC_{71}BM$ in our hybrid solar cells. Because it is difficult for electrons to be transferred from the InP QDs to the $PC_{71}BM$ due to the conduction band level being

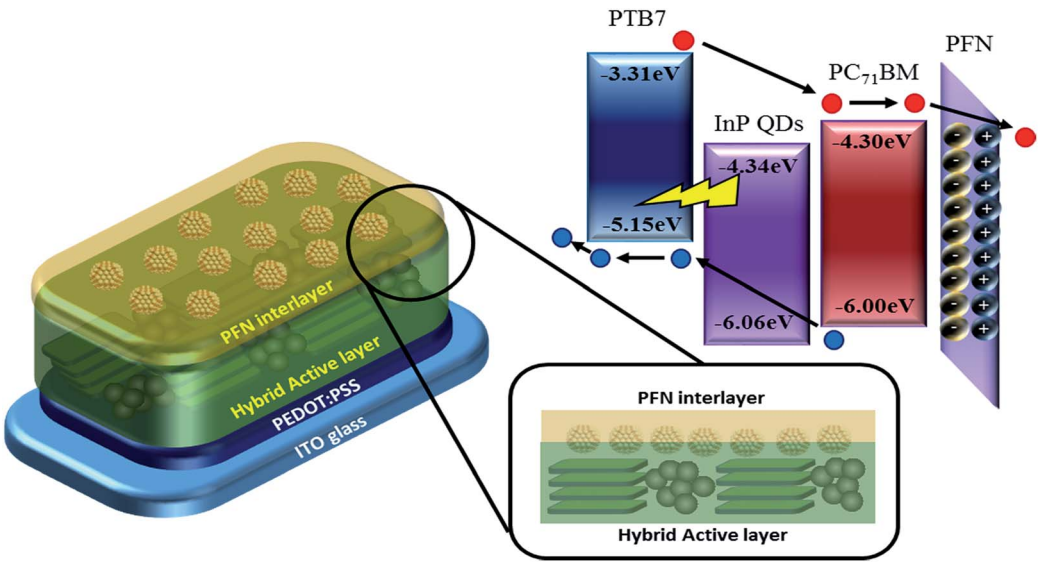

Scheme 1 Schematic image of organic–inorganic hybrid solar cells consisting of PTB7, $PC_{71}BM$, InP QDs and PFN interlayer with energy transfer and charge transfer.

lower than that of $PC_{71}BM$ (LUMO level in the case of $PC_{71}BM$), BHJ solar cells composed of the (InP QDs + $PC_{71}BM$) active layer showed low efficiency (Fig. S2 and Table S1†). InP QDs were distributed on the surface of the active layer after forming a thin film (Fig. 5 and 6). The photon energy coming through the anode was largely absorbed by the PTB7, and the generated carriers. Additionally, extra photon energy was transferred to the PTB7 through the emission ($\lambda_{max} = 650$ nm) of the InP QDs.

Conclusions

In this study, organic–inorganic hybrid solar cells in which 5 wt% InP QDs were added into the BHJ active layer (PTB7 + $PC_{71}BM$) were successfully produced. It was verified that InP QDs were distributed on the surface of the active layer after forming thin films. The photon energy coming through the anode was largely absorbed by PTB7, and the generated carriers and InP QDs increased the overall photocurrent by transferring the extra photon energy to PTB7. The carrier recombination was reduced by the introduction of the PFN interlayer. A device was successfully fabricated that indicated a maximum PCE of 8.4% due to the increase of J_{sc} and FF by the synergy effect of InP QDs and the PFN interlayer.

Acknowledgements

This study was supported by the New & Renewable Energy Core Technology Program of the Korea Institute of Energy Technology Evaluation and Planning (KETEP), granted financial resource from the Ministry of Trade, Industry & Energy, Republic of Korea (No. 20133030000180).

Notes and references

1 N. A. Nismy, K. D. G. I. Jayawardena, A. A. D. T. Adikaari and S. R. P. Silva, *Adv. Mater.*, 2011, **23**, 3796–3800.
2 Y. Liu, J. Zhao, Z. Li, C. Mu, W. Ma, H. Hu, K. Jiang, H. Lin, H. Ade and H. Yan, *Nat. Commun.*, 2014, **5**, 1–8.
3 D. H. Wang, P.-O. Morin, C.-L. Lee, A. K. K. Kyaw, M. Leclercb and A. J. Heeger, *J. Mater. Chem. A*, 2014, **2**, 15052–15057.
4 S. W. Heo, K. H. Baek, H. J. Song, T. H. Lee and D. K. Moon, *Macromol. Mater. Eng.*, 2014, **299**, 353–360.
5 W. Kim, J. K. Kim, E. Kim, T. K. Ahn, D. H. Wang and J. H. Park, *J. Phys. Chem. C*, 2015, **119**, 5954–5961.
6 J. M. Lobez, T. L. Andrew, V. Bulović and T. M. Swager, *ACS Nano*, 2012, **6**, 3044–3056.
7 Z. Tang, W. Tress, Q. Bao, M. J. Jafari, J. Bergqvist, T. Ederth, M. R. Andersson and O. Inganäs, *Adv. Energy Mater.*, 2014, **4**, 1400643.
8 H. J. Song, E. J. Lee, D. H. Kim, T. H. Lee, M. Goh, S. Lee and D. K. Moon, *Dyes Pigm.*, 2015, **113**, 210–218.
9 Z. He, C. Zhong, S. Su, M. Xu, H. Wu and Y. Cao, *Nat. Photonics*, 2012, **6**, 591–595.
10 B. H. Lee, J.-H. Lee, S. Y. Jeong, S. B. Park, S. H. Lee and K. Lee, *Adv. Energy Mater.*, 2015, **5**, 1401653.
11 E. J. Lee, S. W. Heo, Y. W. Han and D. K. Moon, *J. Mater. Chem. C*, 2016, **4**, 2463–2469.
12 J. P. Han, E. J. Lee, Y. W. Han, T. H. Lee and D. K. Moon, *J. Ind. Eng. Chem.*, 2016, **36**, 44–48.
13 H. Zhou, Y. Zhang, C. K. Mai, J. Seifter, T. Q. Nguyen, G. C. Bazan and A. J. Heeger, *ACS Nano*, 2015, **9**, 371–377.
14 T. Liu, L. Huo, X. Sun, B. Fan, Y. Cai, T. Kim, J. Y. Kim, H. Choi and Y. Sun, *Adv. Energy Mater.*, 2015, 1502109.
15 L. Lu, W. Chen, T. Xu and L. Yu, *Nat. Commun.*, 2015, **6**, 7327.
16 Y. (Michael) Yang, W. Chen, L. Dou, W.-H. Chang, H.-S. Duan, B. Bob, G. Li and Y. Yang, *Nat. Photonics*, 2015, **9**, 190–198.
17 H. Kang, S. Kee, K. Yu, J. Lee, G. Kim, J. Kim, J.-R. Kim, J. Kong and K. Lee, *Adv. Mater.*, 2015, **27**, 1408–1413.
18 C.-C. Chen, W.-H. Chang, K. Yoshimura, K. Ohya, J. You, J. Gao, Z. Hong and Y. Yang, *Adv. Mater.*, 2014, **26**, 5670–5677.
19 F. Guo, P. Kubis, N. Li, T. Przybilla, G. Matt, T. Stubhan, T. Ameri, B. Butz, E. Spiecker, K. Forberich and C. J. Brabec, *ACS Nano*, 2014, **8**, 12632–12640.
20 M. Nam, J. Park, S. Kim and K. Lee, *J. Mater. Chem. A*, 2014, **2**, 3978–3985.
21 Y. Zhao, H. Li, X.-J. Liu, L.-L. Guan, Y.-L. Li, J. Sun, Z.-F. Ying, J.-D. Wu and N. Xu, *Nanoscale Res. Lett.*, 2014, **1**, 308.
22 C. Liu, J. Li, X. Zhang, Y. He, Z. Li, H. Li, W. Guo, L. Shen and S. Ruan, *Phys. Chem. Chem. Phys.*, 2015, **17**, 7960–7965.
23 W. Luo, T. Jiu, C. Kuang, B. Li, F. Lu and J. Fang, *Nano Res.*, 2015, **8**, 3045–3053.
24 K. L. Chopra, P. D. Paulson and V. Dutta, *Prog. Photovolt.: Res. Appl.*, 2004, **12**, 69–92.
25 S. Chander and M. S. Dhaka, *Mater. Sci. Semicond. Process.*, 2015, **40**, 708–712.
26 X. Cao, Y. Yamaguchi, Y. Ninomiya and N. Yamada, *J. Appl. Phys.*, 2016, **119**, 025104.
27 K. W. Song, R. Costi and V. Bulović, *Adv. Mater.*, 2013, **25**, 1420–1423.
28 I. J. Kramer and E. H. Sargent, *ACS Nano*, 2011, **5**, 8506–8514.
29 J. Albero, J. N. Clifford and E. Palomares, *Coord. Chem. Rev.*, 2014, **263–264**, 53–64.
30 P. V. P. Kamat, *J. Phys. Chem. Lett.*, 2013, **4**, 908–918.
31 G. Kim, H. Kim, B. Walker, H. Choi, C. Yang, J. Park and J. Y. Kim, *ACS Appl. Mater. Interfaces*, 2013, **5**, 1757–1760.
32 C.-H. M. Chuang, P. R. Brown, V. Bulović and M. G. Bawendi, *Nat. Mater.*, 2014, **13**, 796–801.
33 M. Yuan, O. Voznyy, D. Zhitomirsky, P. Kanjanaboos and E. H. Sargent, *Adv. Mater.*, 2015, **27**, 917–921.
34 Y. Liang, Z. Xu, J. Xia, S. T. Tsai, Y. Wu, G. Li, C. Ray and L. Yu, *Adv. Mater.*, 2010, **22**, 135–138.
35 L. Lu and L. Yu, *Adv. Mater.*, 2014, **26**, 4413–4430.
36 P. Mushonga, M. O. Onani, A. M. Madiehe and M. Meyer, *J. Nanomater.*, 2012, 1–11.
37 S. Braun, W. R. Salaneck and M. Fahlman, *Adv. Mater.*, 2009, **21**, 1450–1472.
38 T. Yang, Z. Jiang, X. Huang, H. Wei, J. Yuan, W. Yue, Y. Li and W. Ma, *Org. Electron.*, 2013, **14**, 2184–2191.
39 U. T. D. Thuy, T. T. T. Huyen, N. Q. Liem and P. Reiss, *Mater. Chem. Phys.*, 2008, **112**, 1120–1123.
40 D. Kiriya, M. Zheng, R. Kapadia, J. Zhang, M. Hettick, Z. Yu, K. Takei, H. H. Hank Wang, P. Lobaccaro and A. Javey, *J. Appl. Phys.*, 2012, **112**, 123102–123111.

41 V. Nandwana, B. Fitzpatrick, Q. Liu, K. M. Solntsev, X. Yu, G. Y. Tonga, S. Eymur, M. Tonga, G. Cooke and V. M. Rotello, *Polym. Chem.*, 2012, **3**, 3072.
42 C. Liu, K. Chang, W. Guo, H. Li, L. Shen, W. Chen and D. Yan, *Appl. Phys. Lett.*, 2014, **105**, 073306.
43 W. Huang, L. Li, G. Hui, D. Chen and A. Zhong, *J. Appl. Polym. Sci.*, 2013, **129**, 1256–1263.
44 Z. He, C. Zhong, X. Huang, W. Y. Wong, H. Wu, L. Chen, S. Su and Y. Cao, *Adv. Mater.*, 2011, **23**, 4636–4643.
45 H. Choi, S. Ko, T. Kim, P.-O. Morin, B. Walker, B. H. Lee, M. Leclerc, J. Y. Kim and A. J. Heeger, *Adv. Mater.*, 2015, **27**, 3318–3324.
46 Z. He, C. Zhang, X. Xu, L. Zhang, L. Huang, J. Chen, H. Wu and Y. Cao, *Adv. Mater.*, 2011, **23**, 3086–3089.
47 G. Dennler, M. C. Scharber and C. J. Brabec, *Adv. Mater.*, 2009, **21**, 1323–1338.
48 J. D. Servaites, M. a. Ratner and T. J. Marks, *Appl. Phys. Lett.*, 2009, **95**, 163302.
49 M. Padilla, B. Michl, B. Thaidigsmann, W. Warta and M. C. Schubert, *Sol. Energy Mater. Sol. Cells*, 2014, **120**, 282–288.
50 W.-J. Ho, Y.-Y. Lee and S.-Y. Su, *Nanoscale Res. Lett.*, 2014, **9**, 483.
51 C. V. Hoven, A. Garcia, G. C. Bazan and T. Q. Nguyen, *Adv. Mater.*, 2008, **20**, 3793–3810.
52 K. Zhang, Z. Hu, R. Xu, X.-F. Jiang, H.-L. Yip, F. Huang and Y. Cao, *Adv. Mater.*, 2015, **27**, 3607.
53 C.-M. Liu, C.-M. Chen, Y.-W. Su, S.-M. Wang and K.-H. Wei, *Org. Electron.*, 2013, **14**, 2476–2483.
54 K. Vandewal, K. Tvingstedt, A. Gadisa, O. Inganäs and J. V. Manca, *Nat. Mater.*, 2009, **8**, 904–909.
55 H. Azimi, A. Senes, M. C. Scharber, K. Hingerl and C. J. Brabec, *Adv. Energy Mater.*, 2011, **1**, 1162–1168.
56 R. Steyrleuthner, M. Schubert, F. Jaiser, J. C. Blakesley, Z. Chen, A. Facchetti and D. Neher, *Adv. Mater.*, 2010, **22**, 2799–2803.
57 S. Honda, H. Ohkita, H. Benten and S. Ito, *Adv. Energy Mater.*, 2011, **1**, 588–598.
58 S. W. Heo, K. W. Song and D. K. Moon, *RSC Adv.*, 2014, **4**, 6776–6781.
59 M. Ramar, C. K. Suman, R. Manimozhi, R. Ahamad and R. Srivastava, *RSC Adv.*, 2014, **4**, 32651.
60 M. Nam, J. Park, K. Lee, S.-W. Kim, H. Ko, I. K. Han and D.-H. Ko, *J. Mater. Chem. A*, 2015, **3**, 10585–10591.